Chem Catalysis

CellPress

Article

Do multinuclear 3d metal catalysts achieve O–O bond formation via radical coupling or via water nucleophilic attack? WNA leads the way in $[Co_4O_4]^{n+}$

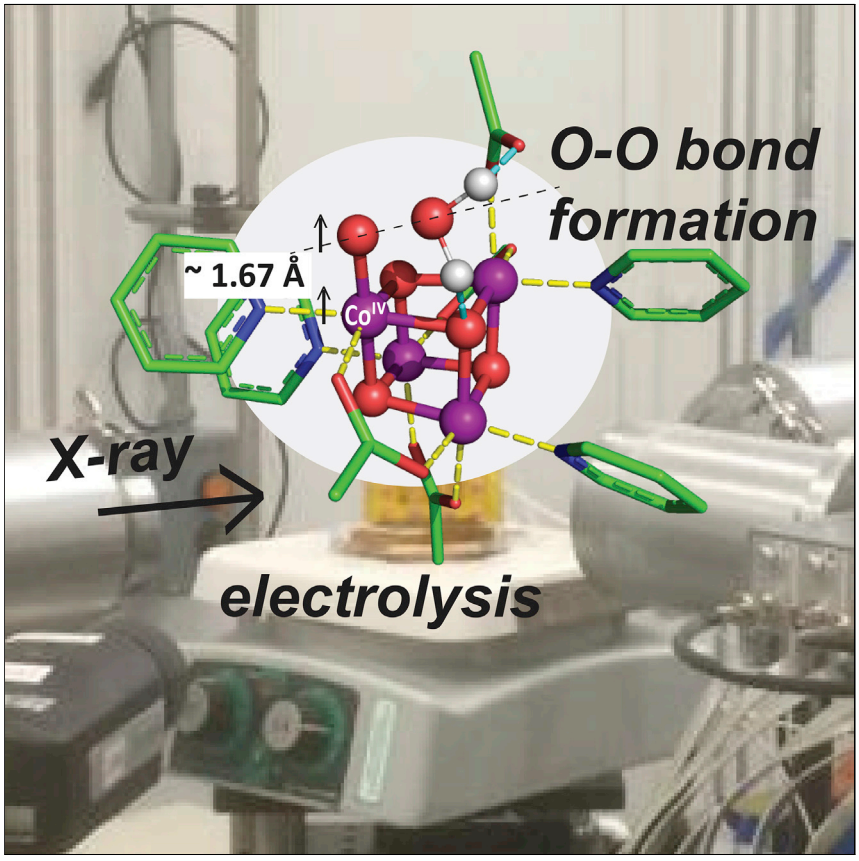

Roman Ezhov, Alireza Karbakhsh Ravari, Gabriel Bury, Paul F. Smith, Yulia Pushkar

ypushkar@purdue.edu

Highlights

In situ EXAFS of $[Co_4O_4]^{4+}$-catalyzed O_2 evolution detects ultrashort ~1.67 Å Co^{IV}=O

Calculations show that Co^{IV}=O has radicaloid character that facilitates interaction with water

Proposed model of water oxidation explains all currently available spectroscopic results

The "oxo wall" is mitigated here by the multimetallic nature of the $[Co_4O_4]$ catalyst

Ezhov et al., Chem Catalysis 1, 1–16
July 15, 2021
https://doi.org/10.1016/j.checat.2021.03.013

Please cite this article in press as: Ezhov et al., Do multinuclear 3d metal catalysts achieve O–O bond formation via radical coupling or via water nucleophilic attack? WNA leads the way in $[Co_4O_4]^{n+}$, Chem Catalysis (2021), https://doi.org/10.1016/j.checat.2021.03.013

Chem Catalysis

CellPress

Article

Do multinuclear 3d metal catalysts achieve O–O bond formation via radical coupling or via water nucleophilic attack? WNA leads the way in $[Co_4O_4]^{n+}$

Roman Ezhov,[1] Alireza Karbakhsh Ravari,[1] Gabriel Bury,[1] Paul F. Smith,[2] and Yulia Pushkar[1,3,*]

SUMMARY

Catalytic water oxidation is a required process for clean energy production based on the concept of artificial photosynthesis. Here, we provide *in situ* spectroscopic and computational analysis for the closest known photosystem II analog, $[Co_4O_4]^{n+}$ ($[Co_4O_4Py_4Ac_4]^0$, Py = pyridine and Ac = CH_3COO^-), which catalyzes electrochemical water oxidation. *In situ* extended X-ray absorption fine structure detects an ultrashort, Co^{IV}=O (~1.67 Å) moiety, a crucial intermediate for O–O bond formation. Density function theory analyses show that the intermediate has two Co^{IV} centers and a Co^{IV}=O unit of strong radicaloid character sufficient to support a Co^{IV}=O + H_2O = Co–OOH + H^+ transition, where the carboxyl ligand accepts the proton and the bridging oxygen stabilizes the peroxide via hydrogen bonding. The proposed water nucleophilic attack mechanism accounts for all prior spectroscopic evidence on the $Co_4O_4^{4+}$ core. Our results are important for the design and development of efficient water oxidation catalysts, which contribute to the ultimate goal of clean energy from artificial photosynthesis.

INTRODUCTION

The oxidation of water is a key half-reaction necessary for supporting a variety of reduction processes such as H_2 or methanol production, CO_2 reduction, and nitrogen fixation.[1] These processes are needed to produce sustainable carbon-neutral fuels and support a CO_2-neutral chemical industry. The oxygen-evolving half-reaction is accomplished in nature via the $CaMn_4O_5$ heterocubane oxygen-evolving complex (OEC) of photosystem II (PS II), and the ultimate goal in the design of artificial photosynthesis water oxidation catalysts is to develop a catalyst with comparable efficiency. Currently, water oxidation electrocatalysts consist of noble-metal oxides, such as IrO_2 and RuO_2, because of their high stability in acid, small overpotential, and low Tafel value.[2,3] However, the application of precious-metal-based catalysts on an industrial scale is cost prohibitive. To make this process more economically viable, oxygen evolution and reduction catalysts have been developed with Earth-abundant metals.[4–9] Water oxidation reaction (WOR) electrocatalysts based on transition-metal oxides have been extensively studied.[10–12]

Cobalt (Co) cubanes bearing the $[Co_4O_4]^{n+}$ oxo-metalate cluster have been of substantial interest for several reasons: (1) structural similarity to the heterocubane OEC responsible for water oxidation in natural photosynthesis[7,13–16], (2) representation of a single, partial unit cell matching the structural motif of several crystalline heterogeneous water oxidation Co-based catalysts, such as Co_3O_4 and $LiCoO_2$,[17–20] and (3) a widely used model structure for the highly active amorphous "Co-Pi" Co oxide

The bigger picture

With increasing energy demand, widespread implementation of water splitting to H_2 is of critical importance for artificial photosynthesis and sustainability, but the oxidation half-reaction $2H_2O \rightarrow O_2 + 4e^- + 4H^+$ requires either an energy input that is too high (high overpotential) or the use of expensive precious metals. The development of fast, inexpensive, and durable water oxidation catalysts (WOCs) is necessary for future sunlight-to-chemical-fuel devices.

Cobalt-oxide-based WOCs comprising the Co_4O_4 cubane motif are currently the systems most structurally and functionally close to the oxygen evolving complex (Mn_4CaO) of photosystem II active in nature. For future development, an exact mechanism of water splitting should be clarified. Here, we present an experimental detection of a Co^{IV}=O moiety during water oxidation with a $Co_4O_4Py_4Ac_4$ molecular catalyst. This observation, supported by density functional theory modeling, develops an understanding of the water nucleophilic attack mechanism in this material.

Please cite this article in press as: Ezhov et al., Do multinuclear 3d metal catalysts achieve O–O bond formation via radical coupling or via water nucleophilic attack? WNA leads the way in $[Co_4O_4]^{n+}$, Chem Catalysis (2021), https://doi.org/10.1016/j.checat.2021.03.013

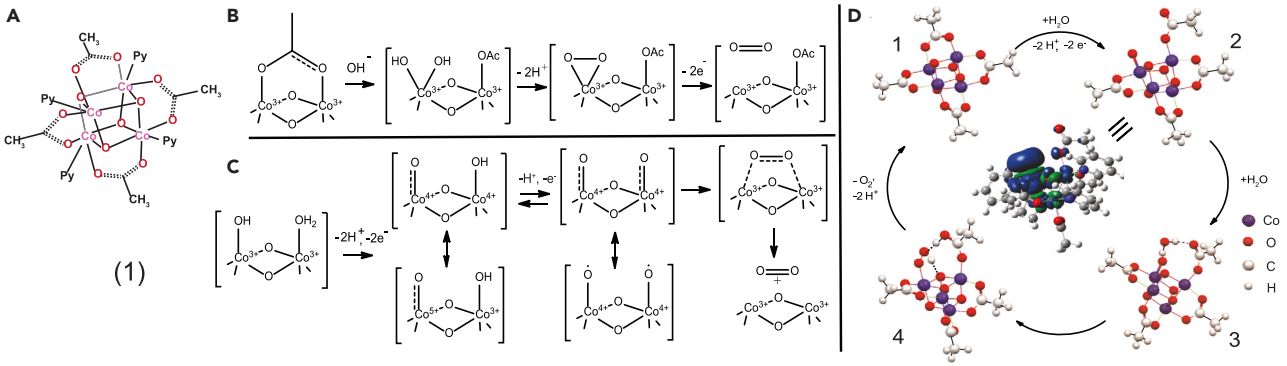

Figure 1. O–O bond formation in Co_4O_4 cubane

(A) Structure of the $[Co_4O_4Py_4Ac_4]^0$ (**1**) water oxidation catalyst.

(B) O–O bond formation via the geminal hydroxide on the Co center.

(C) O–O bond formation via radical coupling at adjacent Co centers in the high oxidation state.

(D) Water nucleophilic attack mechanism proposed in this study of (**1**)-catalyzed WOR during bulk electrolysis at pH 12. In the middle is the DFT model of the $[Co^{III}_2O_4Co^{IV}{=}O/Co^{IV}(CH_3CO_2)_{mono}]^0$ active intermediate with a spin-density distribution showing the strong radicaloid character of the $Co^{IV}{=}O$ unit. Peroxide formation is facilitated by two H bonds, such that the carboxyl accepts a proton and a bridging oxygen stabilizes the peroxide.

catalyst.[7,21–25] The question of whether the single, molecular cubane is itself a catalyst has been affirmatively answered only recently for $[Co_4O_4Py_4Ac_4]^0$ (**1**) (Figure 1A) given that studies reported prior to 2014 were found to be affected by the presence of catalytically active impurities.[26] Since the report of the purification procedure, the Tilley[27] and Dismukes[28] groups both showed that (**1**) was able to promote WOR only at basic pH (pH ~12) because the crucial process necessary for the one-electron oxidized $[Co_4O_4(OAc)_4(py)_4]^+$ $(\mathbf{1})^+$ inducing a WOR catalytic cycle is coordination of the hydroxyl ion (OH^-) to its Co center. The likely molecular nature of O_2 evolution from (**1**) in photocatalytic assays was also shown by Genoni et al.[29] and, more recently, in an *operando* spectroscopy study by Liu and Frei,[30] who detected the O–O intermediate. Elucidating the mechanism of the O–O bond formation in such catalysts is crucial to the development of artificial photosynthesis.

Catalytic mechanisms of (**1**) have been studied with UV-visible spectroscopy, electron paramagnetic resonance (EPR), mass spectrometry, X-ray spectroscopy, density functional theory (DFT) calculations, and O_2 evolution measurements at different pH and isotopically labeled reagents.[27,28,31,32] Different conformations of the mixed Co^{IV}/Co^{III} cubane intermediates and the O–O-forming units of molecular Co-based catalysts have been discussed previously (Figures 1B and 1C).[20,23,28,30,32–35] Several assumptions about the architecture of the $[Co_4O_4]^{n+}$ cluster bearing highly oxidized Co=O species during WOR have been made (Figure 1C), and a majority of works propose participation of the neighboring Co–Co di-μ-oxo moieties in high oxidation states (presumably $Co^{IV}{=}O$) during the formation of peroxo species and O_2 release (Figure 1C). Generally, formation of the high-valent metal-oxo species is considered a key factor in catalyst activation for oxidation reactions, including WOR.[36–42]

Mechanistic observations and proposals are more diverse for different metal-oxide systems. Here, both water nucleophilic attack (WNA) and radical coupling (RC) were widely considered. For instance, the formation of Fe=O species followed by WNA is claimed to be responsible for the water oxidation activity of iron-oxide-based WOCs.[43–46] The peroxo intermediates of Co oxides, bearing a $[Co_4O_4]$ structural unit, were detected by different infrared (IR) spectroscopic techniques.[30,37] In addition to the Co^{IV}/Co^{IV} formation followed by RC to form the peroxo unit,[23,47] the

[1]Department of Physics and Astronomy, Purdue University, West Lafayette, IN 47907, USA

[2]Department of Chemistry, Valparaiso University, Valparaiso, IN 46383, USA

[3]Lead contact

*Correspondence: ypushkar@purdue.edu

https://doi.org/10.1016/j.checat.2021.03.013

possibilities of Co^{III}/Co^{V} and cofacial hydroxo-oxo species $Co^{III}(OH)/Co^{IV}$ have been considered.[23,32,48] A similar conformational motif of edge-site catalysis was proposed for the electrocatalytic intermediates of the Co oxides and Co-Pi catalytic films.[33–35] This literature overview shows that, in contrast to diverse mechanistic proposals in heterogeneous systems, a mechanism consisting of RC significantly dominates the discussion of the catalytic activity of the molecular cubane (**1**). Reactivity proposals that would prefer a WNA instead are limited to calculations[7] or only partially supported.[30] Alternatively, the possible formation of a side-on peroxo unit on a Co^{III} metal center (geminal 1,1-intermediate) was concluded after the lack of activity of its bpy (2,2′-bipyridine) analog, where such a conformation is impossible (Figure 1B). This mechanism suggests that after OH^--promoted hydrolysis of the Co–OAc site, formation of the $Co(OH)_2$ intermediates occurs. Then, these 1,1-(gem)-dihydroxo species undergo oxidation by $(\mathbf{1})^+$, followed by O_2 release.[28]

Although the formation of Co^{IV}=O species as a key intermediate was hypothesized in all of the mechanistic schemes for (**1**) (Figure 1C), these oxo species have never been observed previously. Here, we present *in situ* X-ray absorption spectroscopy (XAS) and extended X-ray absorption fine structure (EXAFS) detection of the Co^{IV}=O fragment, supported by EPR and DFT analysis, to uncover the structure of the reactive intermediates in WOR catalyzed by (**1**). Co=O species are extremely elusive, highlighting the concept of the "oxo wall," an empirical observation of the scarcity of M=O (M is a transition metal) complexes beyond group 8 of the periodic table. These species have been reported only in exceptional cases, mostly in pyrolytic transformations of Co-based complexes.[23,37–41] Our direct observation confirms the generation of the Co^{IV}=O intermediate in WOR promoted by (**1**); subsequent DFT and EPR analysis highlights its ability to directly activate water via WNA, a new mechanistic observation for the field. We also compare the $[Co_4O_4]^{n+}$ unit to the OEC of PS II during WOR.

RESULTS AND DISCUSSION

In situ XAS

In this study, we determined the presence of the Co^{IV}=O intermediate by using *in situ* X-ray absorption near-edge structure (XANES) and EXAFS during electrochemical WOR of purified (**1**) at 1.4 V versus Ag/AgCl potential in a basic water solution (pH 12) for a prolonged time (8 h) (Figures 2A and 2B and Table S1). While rate law studies for (**1**) have been performed down to pH 11, the hydroxide contribution to the rate law renders the reaction too kinetically slow below this value. Thus, in agreement with earlier mechanistic studies of (**1**), pH 12 was used. XAS measurements were performed for (1) initial (**1**), (2) (**1**) oxidized under noncatalytic conditions with cerium(IV) ammonium nitrate (Ce^{IV}) at pH 1 (measured at 20 K) (Figure S1), and for the first time, (3) under catalytic conditions via *in situ* bulk electrolysis (BE) of (**1**) at pH 12 (Figures 2A and 2B). All the necessary controls were done to ensure that catalytic current was caused by the presence of (**1**), and in particular, the baseline current without (**1**) was ~10 times lower, and the working electrode after the BE experiment was Co free by X-ray fluorescence, in agreement with prior electrocatalysis studies of the purified cubane[27]. Experiments were done during multiple beam times to ensure reproducibility. The resulting data show a shift to higher energy and shape change of the Co K-edge (Figures 2A and S1) under both catalytic and noncatalytic oxidation. No changes in multiple EXAFS scans of the initial solution prior to the BE were observed. This indicates no detectable X-ray-induced photodecomposition of the catalyst under the defocused X-ray beam used in the study.[49] In addition, no precipitate or film deposition was observed on the X-ray beam pathway during BE.

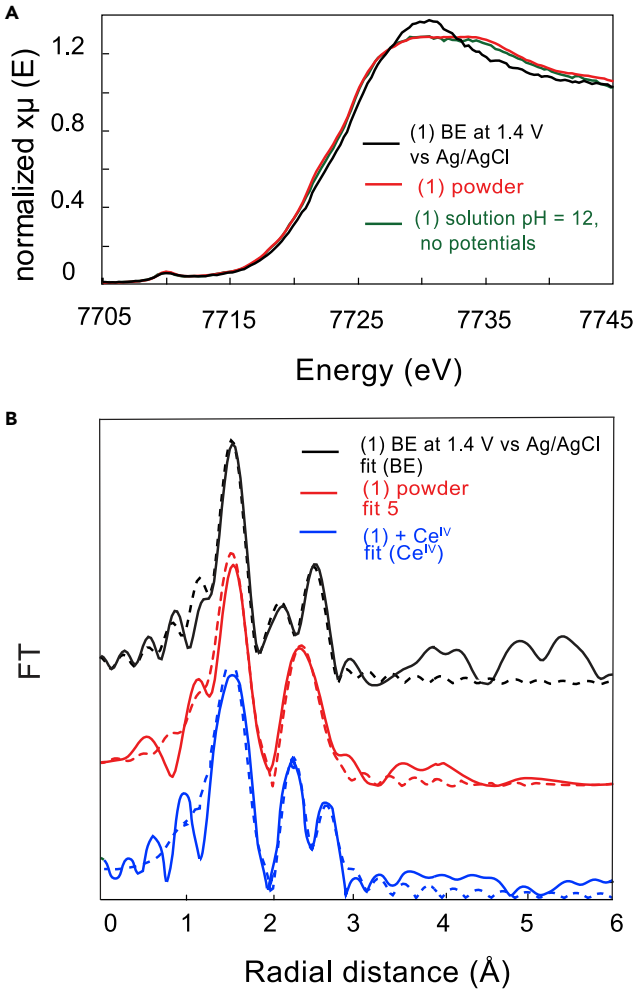

Figure 2. XAS spectroscopy of (1) and its oxidized intermediates

(A) Co K-edge XANES of (**1**) as a starting powder (red), its solution at pH 12 before BE electrolysis (green), and its solution during the electrolysis at pH 12 with 1.4 V potential versus Ag/AgCl after prolonged time (black).

(B) EXAFS data and corresponding best fits (dashed lines; Tables S1 and S3) of (**1**) as a powder (red), its solution during BE electrolysis (black), and its solution oxidized with Ce^{IV} (blue) and measured in a cryostat (20 K).

Compound (**1**) contains four Co^{III} ions, whereas $(\mathbf{1})^+$ has a single Co^{IV}, which translates to an ~0.4 eV positive shift in Co K-edge XANES[36] (Figure S1). However, the Co K-edge XANES measured during BE of (**1**) in water at pH 12 (Figure 2A) has ~1 eV K-edge shift compared with the dissolved, all-Co^{III} cubane. This is consistent with the formation of a $[Co^{III}_2Co^{IV}_2]$ intermediate, comparable to that reported earlier for electrolysis in CH_3CN.[23] Oxidation of $(\mathbf{1})^+$ to the $[Co^{III}_2Co^{IV}_2O_4]^{2+}$ state is predicted from DFT calculations to take place at approximately +1.4–1.5 V (Tables S2 and S3) in nonprotic solvents and was reproduced here with experimental cyclic voltammetry data (Figure S3). In addition, the XANES spectral shape changes, with the top of the edge becoming pointier (Figure 2A). This change indicates a potential geometric change in the cluster and change in the form of the cluster frontier's orbitals. EPR analysis of the samples quickly frozen in liquid N_2 from the *in situ* cell during prolonged BE under applied potential indicates mostly EPR-silent species,

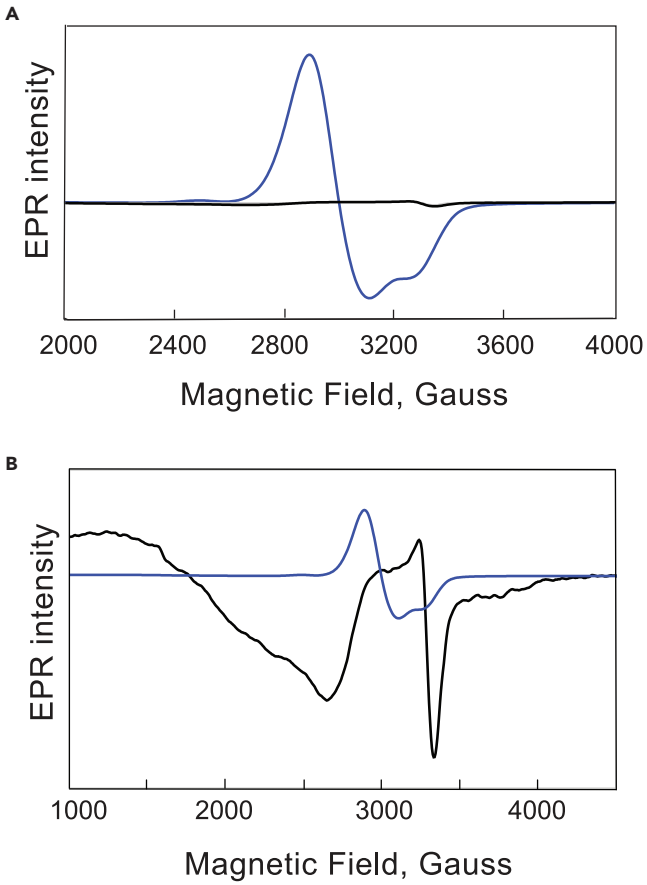

Figure 3. X-band EPR at 20 K

(A) 1 mM solution of $(\mathbf{1})^+$ (blue) in comparison with 1 mM solution of (**1**) (black) subjected to BE at pH 12 with 1.4 V potential versus Ag/AgCl after prolonged time (black) and quickly frozen for EPR analysis. The spectra are presented on the same intensity scale.

(B) The same comparison but the EPR intensity of the BE sample is magnified 100 times.

agreeing with the $[Co^{III}{}_2Co^{IV}{}_2]$ oxidation state assignment (Figures 3A and 3B) (see below for a detailed description of the EPR results).

EXAFS analysis indicates considerable changes in the structure of (**1**) at pH 12 and the applied potential (Figure 2B). Note that EXAFS data were collected in an extended k > 15 $Å^{-1}$ range to ensure the best distance resolution. EXAFS fits of the initial (**1**) and $(\mathbf{1})^+$ formed by Ce^{IV} oxidation agree with known structures of these species (Table S4, Figure S2). The first coordination sphere of Co comprises oxygens as μ_3-oxo bridges, expected Co–O at ~1.85 Å, and a single nitrogen ligand from pyridine with Co–N at ~1.90 Å. However, to achieve satisfactory EXAFS fits of the *in situ* data, the addition of a short ~1.65–1.70 Å Co–O vector is required (Table S1). This distance agrees well with the DFT model of $[Co^{III}{}_2O_4Co^{IV}{=}O/Co^{IV}(CH_3CO_2)_{mono}]^0$ (Tables 1 and S5, Figure 1D) and is comparable to the shortest Co=O bond length isolated to date at 1.72 Å.[39] For Co–O at ~1.67 Å, both n = 0.25 and n = 0.5 vectors give similar fit results. Note that N is not a coordination number but a parameter of the EXAFS fit, which is defined as n = (number of Co-X vectors)/(number of Co ions in the molecule). Thus, n = 0.25 corresponds to the presence of a single Co^{IV}=O unit per $[Co_4O_4]^{n+}$, while n = 0.5 would require two Co^{IV}=O units per $[Co_4O_4]^{n+}$. EXAFS fits cannot distinguish whether the intermediate has one or two Co^{IV}=O units, while a

Please cite this article in press as: Ezhov et al., Do multinuclear 3d metal catalysts achieve O–O bond formation via radical coupling or via water nucleophilic attack? WNA leads the way in $[Co_4O_4]^{n+}$, Chem Catalysis (2021), https://doi.org/10.1016/j.checat.2021.03.013

Table 1. DFT analysis of O–O bond formation by $(1)^{2+}$ ($Co^{III}_2Co^{IV}_2$) state of the Co_4O_4-cubane

Reactions of O–O bond formation	ΔG (eV)
BP86	
$^{T}Co^{III}_2O_4Co^{IV}$=O/$Co^{IV}(CH_3CO_2)_{mono}$ + H_2O = $^{S}Co^{III}_2O_4Co^{III}$–OOH/$Co^{III}(CH_3CO_2H)_{mono}$	+0.92
$^{T}Co^{III}_2O_4Co^{IV}$=O/$Co^{IV}(CH_3CO_2)_{mono}$/H_2O = $^{S}Co^{III}_2O_4Co^{III}$–OOH/$Co^{III}(CH_3CO_2H)_{mono}$	+1.12
$^{T}Co^{III}_2O_4Co^{IV}$=O/$Co^{IV}(CH_3CO_2)_{mono}$ = $^{S}Co^{III}_3O_4Co^{III}(OOC(O)CH_3)_{bridging}$	+0.56
$^{T}Co^{III}_2O_4Co^{IV}$=O/$Co^{IV}(CH_3CO_2)_{mono}$/H_2O/OH^- = $^{S}Co^{III}_2O_4Co^{III}$–OOH/$Co^{III}(CH_3CO_2)_{mono}$/$H_2O$	−0.61
BP86 with 15% Hartree Fock	
$^{T}Co^{III}_2O_4Co^{IV}$=O/$Co^{IV}(CH_3CO_2)_{mono}$ + H_2O = $^{S}Co^{III}_2O_4Co^{III}$–OOH/$Co^{III}(CH_3CO_2H)_{mono}$	−0.55
$^{T}Co^{III}_2O_4Co^{IV}$=O/$Co^{IV}(CH_3CO_2)_{mono}$/H_2O = $^{S}Co^{III}_2O_4Co^{III}$–OOH/$Co^{III}(CH_3CO_2H)_{mono}$	−0.19
Additional oxidation reactions	Redox potential (eV)
$^{T}Co^{III}_2O_4Co^{IV}$=O/$Co^{IV}(CH_3CO_2)_{mono}$/H_2O = $^{D}Co^{III}O_4Co^{IV}$=O/Co^{IV}, $Co^{IV}(CH_3CO_2)_{mono}$/H_2O + e^-	+0.86
$^{S}Co^{III}_2O_4Co^{III}$–OOH/$Co^{III}(CH_3CO_2H)_{mono}$ = $^{D}Co^{III}_2O_4Co^{IV}$–OOH/$Co^{III}(CH_3CO_2H)_{mono}$ + e^-	+0.12

higher number of units is unlikely. A DFT model for $Co^{III}_2O_4Co^{IV}$=O/Co^{IV}=O species (Figure 1C and Tables 1 and S5), widely discussed in mechanistic proposals as the one forming a O–O bond via an RC mechanism, does not agree with our EXAFS results, as it predicts Co–O at ~1.75 Å (see Table S1). Thus, combined spectroscopic and DFT data indicate a strong preference for a single Co^{IV}=O unit per $[Co_4O_4]^{n+}$ due to (1) energetic penalty of complete acetate ligand dissociation (see "DFT analysis" and Equation S1), (2) discrepancy in the Co–O bond length for species with two Co-oxo, and (3) lack of experimental observation of full acetate dissociation. From our prior experience, fitting short metal-oxygen distances to EXAFS data that do not have such interactions always results in worse fits. For instance, fitting a Co=O vector at ~1.7 Å to initial (1) or to $(1)^+$ resulted in significantly worse fits (data not shown). Our DFT analysis (below) shows that one Co^{IV}=O fragment per $[Co_4O_4]^{n+}$ may enable O–O bond formation. DFT of a $[Co^{III}_2O_4Co^{IV}$=O/$Co^{IV}(CH_3CO_2)_{mono}]^0$ model (Figure 1D, intermediate 2) also predicts two groups of Co–Co distances: one shorter (~2.73 Å) and one longer (~2.86–2.91 Å). EXAFS fits improve if the Co–Co vector is split into two shells (Table S1).

In situ EPR

Oxidation of (1) by one electron results in the well-known paramagnetic (S = 1/2) cubium signal $(1)^+$.[28] This signal can be produced by oxidation with Ce^{IV} at acidic pH or by BE at neutral pH ~ 7, where the catalyst is inactive (Figure S5). EPR samples from BE in pH 12 solution at 1.4 V versus Ag/AgCl electrode (concentration of (1) 1 mM) were quickly frozen and compared by X-band EPR at 20 K with solution of $(1)^+$ of the same concentration (Figures 3A and 3B). BE samples were largely EPR silent (lost at least ~90% of the EPR signal; only one sample is shown in Figure 3A), except for the background, due to frozen oxygen, which evolves vigorously under BE conditions, and new signal described below (can be seen under 100× magnification). Loss of S = 1/2 EPR signal is consistent with XAS data, ensuring oxidation to the $(1)^{2+}$ state. $(1)^{2+}$ can have an EPR-undetectable $[Co^{III}_2O_4Co^{IV}$=O/$Co^{IV}(CH_3CO_2)_{mono}]^0$ form (S = 0 or S = 1; Table S5), as discussed below, based on XAS analysis and DFT. Traces of cubium $(1)^+$ signal are detected upon sample melting (data not shown). A zoomed view (×100 magnification) into the black curve in Figure 3A shows a new, short-lived (as it disappears with sample melting) S = 1/2 signal (Figure 3B, black). The signal maximum is at g ~ 2.08 and has a g_{zz} component centered around g ~ 1.80. The g-tensor values near g ~ 2 indicate a significant electron localization on the ligand. Low g-tensor values were previously reported for Co^{III}–O_2^- superoxo complexes.[50–52] We cannot exclude that additional structure in the signal, in particular around g_{zz}, belongs to a rather large (50–60 G) ^{59}Co (I = 7/2) hfs. Low content (a few percent) of the signal, large frozen O_2 backgrounds due to high activity of this catalyst, and the short-lived nature of this new S = 1/2 signal

prevented its further analysis. Currently, we cannot exclude that two EPR signals can be present in this range with different ^{59}Co (I = 7/2) hyperfine splitting. For completeness, below we provide DFT computed ^{59}Co hfs and show that large ^{59}Co (I = 7/2) hfs is possible for Co^{IV}–OOH terminal peroxo species.

DFT analysis

It is experimentally established that $Co^{III}_2Co^{IV}_2$ is a catalytically competent state. Multiple potential mechanisms for O–O formation by $[Co_4O_4]^{n+}$ cubane have been discussed (Figures 1B and 1C).[13,14,23,27,28,31,36,53] The experimental consensus that bridging oxygens do not exchange under catalytic conditions suggests that O–O bond formation involving bridging oxygens should not be considered.

The $[Co^{III}_2Co^{IV}_2]^{2+}$ cubane generated in nonaqueous solutions can be in a triplet (S = 1) or a singlet state (S = 0), which are energetically equal.[23] *In situ* XANES at pH 12 in water confirms the $Co^{III}_2Co^{IV}_2$ intermediate. EXAFS data indicate that at pH 12 the intermediate contains at least one Co^{IV}=O group. The minimally modified structure where this group can be achieved is $[Co^{III}_2O_4Co^{IV}{=}O/Co^{IV}(CH_3CO_2)_{mono}]^0$, where the single bridging acetate becomes a terminal ligand (Figure 1D). Prior studies of WNA mechanisms highlighted the benefit of a base (acetate is one example) for structural stabilization and energy lowering via H bonds.[28,54] Intramolecular H bonding was noted as a prevalent stabilizing force for water molecules terminally binding metals in some WOC systems.[55] For the $[Co^{III}_2O_4Co^{IV}{=}O/Co^{IV}(CH_3CO_2)_{mono}]^0$ structure, the triplet state is ~0.7 eV lower in energy than the singlet (Table S5). DFT-computed Co^{IV}=O in this intermediate (~1.675 Å) matches well the Co–O distance (~1.67 Å) detected in EXAFS (Table S1). Differences in Co–O distances computed with three DFT approaches are insignificant (~1.67 Å with BP86, ~1.66 Å with B3LYP, and ~1.61 Å with BP86 + 15% HF). Co–Co distances that are separated into two groups, the shorter (~2.73 Å) and the longer (~2.85 Å), also match the DFT model (Table S1).

A recent time-resolved rapid-scan IR observation of photo-oxidized cubane at pH 12.3 indicates no free acetate under reaction conditions, suggesting that all acetates remain at least as the terminal ligands to the cubane.[30] In the same study, an ~833 cm^{-1} band was assigned to the Co–OO–Co peroxo species bridging two Co centers. These two observations are challenging to reconcile, given that the Co–OO–Co species were proposed following oxidation in water by a cubane having dissociated an acetate, as offered in a recently proposed mechanism.[53] Either the bridging species would need to be generated by isomerization following coordination of second water to an adjacent Co, as offered by Liu and Frei[30], or the 833 cm^{-1} band is an O–O vibration of different geometry.

In considering an alternative, a prior report has shown that the structural analog $[Co_4O_4(bpy)_4Ac_2]^{2+}$ is not an active catalyst under the same conditions; in that interpretation, the proposed mechanism called for a side-on peroxide formation from $Co(OH)_2$ geminal sites (Figure 1B).[28] Notably, the two cubanes do not exhibit similar redox potentials to access $Co^{III}_2Co^{IV}_2$ in acetonitrile solvent[23] (Table S3). Cyclic voltammogram data for (**1**) in acetonitrile has confirmed the earlier result[23] (Figure S3), while in the same electrochemical window the bpy analog reversibly oxidizes only once at approximately +0.71 V.[6,56] Hence, oxidation of the bpy derivative requires greater energy input, likely due to its positive charge. DFT calculations confirm this effect (Table S3). Note that protic solvents are known to form hydrogen (H) bonds to the cubane μ_3-oxos, reducing donation to Co and raising the potentials in aqueous solution.[53] This effect causes (**1**) and the bpy analog to reach the $Co^{III}_3Co^{IV}$ level at

Please cite this article in press as: Ezhov et al., Do multinuclear 3d metal catalysts achieve O–O bond formation via radical coupling or via water nucleophilic attack? WNA leads the way in $[Co_4O_4]^{n+}$, Chem Catalysis (2021), https://doi.org/10.1016/j.checat.2021.03.013

identical potentials in water. Nonetheless, the $Co^{III}_2Co^{IV}_2$ level was observed for (1) and remains undetected for the bpy analog, potentially explaining its lack of catalytic activity without necessarily requiring a geminal, side-on mechanism.

Considering the aforementioned observations and contradictions, we explored the reaction of $[Co^{III}_2O_4Co^{IV}{=}O/Co^{IV}(CH_3CO_2)_{mono}]^0$ with water via the WNA mechanism, which has negative (−0.27 eV) ΔG in the calculations done with 15% Hartree Fock exchange (Tables 1 and S6 and Figure 1D). Multiple research groups have noted that inclusion of a variable percentage of Hartree Fock exchange stabilizes the peroxide species in PS II OEC.[57–59] In O–O bond formation with the $[Co_4O_4]$ cubane, the terminal acetate acts as a proton acceptor group. A barrier of approximately +0.9 eV is estimated for the computed WNA process (Tables S6 and S7, Figure S4, and Video S1; see supplemental information for details). Additional driving force can be provided by proton removal at pH 12 and oxidation of formed $Co^{III}_3O_4Co^{III}$–OOH to $Co^{III}_3O_4Co^{IV}$(OOH). This should require a moderate potential (Table 1) while shifting the equilibrium toward a peroxo form. Direct OH^- hydroxide ion reaction with Co^{IV}=O in $[Co^{III}_2O_4Co^{IV}{=}O/Co^{IV}(CH_3CO_2)_{mono}]^0$ is also thermodynamically possible (Table 1). The ratio of Co^{IV}=O reactivity via direct water (~55 M) activation or via reaction with OH^- (~0.01 M at pH 12) is dependent on the reactant availability and reaction barrier.

Direct involvement of oxygen-containing ligands such as N-oxides and carboxylates into O–O bond formation was proposed for some water oxidation catalysts.[60,61] Currently, experimental confirmation of the direct carboxylate ligand involvement in O–O bond formation is lacking. Nevertheless, for complete analysis of all possible pathways, the $^S[Co^{III}_3O_4Co^{III}(OOC(O)CH_3)_{bridging}]^0$ product of O–O bond formation was computed (Table 1). Energetically, this pathway is similar to WNA but was not further investigated pending experimental evidence.

DFT-computed spectroscopic properties of proposed intermediates are summarized in Table 2. The computed O–OH vibration in $^S[Co^{III}_2O_4Co^{III}$–$OOH/Co^{III}(CH_3CO_2H)_{mono}]^0$ peroxide is ~762 cm^{-1} and is insensitive to O–OH to O–OD exchange (Table 2). Thus, this type of end-on peroxide also agrees with reported Fourier transform infrared (FTIR) spectroscopy.[30] O–OH vibration (~807 cm^{-1}) of the oxidized $[Co^{III}_2O_4Co^{IV}$–$OOH/Co^{III}(CH_3CO_2H)_{mono}]^+$ form is highly plausible under applied potential and agrees better with the FTIR experiment. Deprotonation of carboxylate ligand, plausible at pH 12 (Table S8), shifts the computed O–O vibration further to ~875 cm^{-1} (Table 2). Both $[Co^{III}_2O_4Co^{IV}$–$OOH/Co^{III}(CH_3CO_2H)_{mono}]^0$ and $[Co^{III}_2O_4Co^{IV}$–$OOH/Co^{III}(CH_3CO_2)_{mono}]^+$ result in O–O vibrational frequencies very close (taking into account ~50 cm^{-1} uncertainty of calculations) to the experimentally reported ~833 cm^{-1} frequency.[30] DFT-computed ^{59}Co hyperfine splitting is presented for completeness for S = 1/2 species (Table 2). Considering pH and applied potential, we conclude that $[Co^{III}_2O_4Co^{IV}$–$OOH/Co^{III}(CH_3CO_2)_{mono}]^0$ is a likely peroxo intermediate with spectroscopic properties matching FTIR. DFT predicts a weak driving force for its deprotonation forming $[Co^{III}_2O_4Co^{IV}$–$OO/Co^{III}(CH_3CO_2)_{mono}]^-$ (Table S8). $[Co^{III}_2O_4Co^{IV}$–$OO/Co^{III}(CH_3CO_2)_{mono}]^-$ is predicted to have smaller ^{59}Co hfs on the order of 15–22 G (Table 2) because of the larger spin density localization on the –OO superoxo fragment. This is an end-on peroxo intermediate, while the attempts to produce side-on peroxide have led toward the end-on state.

We computed the bridging peroxide ($Co^{III}_2O_4Co^{III}$–OO–Co^{III}) that was proposed to explain FTIR results,[30] but obtained ~718 cm^{-1}. This O–O bond frequency significantly

Please cite this article in press as: Ezhov et al., Do multinuclear 3d metal catalysts achieve O–O bond formation via radical coupling or via water nucleophilic attack? WNA leads the way in $[Co_4O_4]^{n+}$, Chem Catalysis (2021), https://doi.org/10.1016/j.checat.2021.03.013

Table 2. DFT-computed key spectroscopic characteristics of the reactive intermediates in BE of (1) in water solution at pH 12 at 1.4 V versus Ag/AgCl applied potential

Intermediate (^{59}Co hfs in gauss for S = 1/2 species)	Vibration (HF)	Isotope shift[a]
$^{T}Co^{III}{}_2O_4Co^{IV}$=O/$Co^{IV}(CH_3CO_2)_{mono}$	Co=O: 744 cm^{-1} (1.61 Å)	Co=^{18}O: 713 cm^{-1};
$^{S}Co^{III}{}_2O_4Co^{III}$–OOH/$Co^{III}(CH_3CO_2H)_{mono}$	–O–OH: 762 cm^{-1} (Co–O: 1.86 Å; O–O: 1.41 Å)	–O–OD: 761 cm^{-1}; –^{18}O–OH: 738 cm^{-1}; –^{18}O–^{18}OH: 718 cm^{-1}; –O–^{18}OH: 742 cm^{-1}
$^{S}Co^{III}{}_2O_4Co^{III}$–OOH/$Co^{III}(CH_3CO_2)_{mono}$	–O–OH: 821 cm^{-1}	–
$^{S}Co^{III}{}_2O_4Co^{III}$–OO/$Co^{III}(CH_3CO_2)_{mono}$	–O–OH: 932 cm^{-1}	–
$^{D}Co^{III}{}_2O_4Co^{IV}$–OOH/$Co^{III}(CH_3CO_2H)_{mono}$ (^{59}Co hfs: A_{xx} = 34; A_{yy} = 58; A_{zz} = 78)	–O–OH: 807 cm^{-1}	–O–OD: 809 cm^{-1}; –^{18}O–OH: 782 cm^{-1}; –^{18}O–^{18}OH: 762 cm^{-1}; –O–^{18}OH: 786 cm^{-1};
$^{D}Co^{III}{}_2O_4Co^{IV}$–OOH/$Co^{III}(CH_3CO_2)_{mono}$ (^{59}Co hfs: A_{xx} = 30; A_{yy} = 52; A_{zz} = 75)	–O–OH: 875 cm^{-1}	–O–OD: 873 cm^{-1}; –^{18}O–OH: 849 cm^{-1}; –^{18}O–^{18}OH: 826 cm^{-1}; –O–^{18}OH: 852 cm^{-1}
$^{D}Co^{III}{}_2O_4Co^{IV}$–OO/$Co^{III}(CH_3CO_2)_{mono}$ (^{59}Co hfs: A_{xx} = 16; A_{yy} = 15; A_{zz} = 22)	–O–OH: 1,090 cm^{-1}	–
$^{S}Co^{III}{}_3O_4Co^{III}(OOC(O)CH_3)_{bridging}$	Co–O–O–C: 725 cm^{-1}	Co–^{18}O–O–C: 720 cm^{-1}
$^{S}Co^{III}{}_2O_4Co^{III}$–OO–$Co^{III}$	O–O: 718 cm^{-1}	–
$^{D}Co^{III}{}_2O_4Co^{IV}$–OO–$Co^{III}$ (^{59}Co hfs: A_{xx} = 14; A_{yy} = 11; A_{zz} = 23)[b] (^{59}Co hfs: A_{xx} = 13; A_{yy} = 11; A_{zz} = 23)	O–O: 905 cm^{-1}	–

[a]Isotope shifts were computed for the most promising intermediates.
[b]Two Co centers have large hfs.

deviates from the experimentally reported ~833 cm^{-1} value. The O–O vibration in the oxidized bridging peroxo intermediate $Co^{III}{}_2O_4Co^{IV}$–OO–Co^{III} was computed to be ~905 cm^{-1}. Generation of $Co^{III}{}_2O_4Co^{IV}$=O/Co^{IV}=O (Figure 1C), a precursor of the $Co^{III}{}_2O_4Co^{III}$–OO–Co^{III} bridging peroxide, carries an approximately +2.1 eV penalty when generated from $Co^{III}{}_2O_4Co^{IV}$=O/$Co^{IV}(CH_3CO_2)_{mono}$ (Equation S1). We did not computationally investigate the pathway in Figure 1B, since it requires de-coordination of two acetate ligands from the same Co center. We suggest that statistically it is less probable than de-coordination of just one acetate ligand.

Thus, summarizing the overall spectroscopic and computational data in this and previous studies, the following observations should be noted for $[Co_4O_4]$-catalyzed water oxidation: (1) *in situ* EXAFS data indicate formation of the Co^{IV}=O species during electrocatalytic WOR, (2) lack of free acetate during WOR signifies that acetate groups remain bound to the Co centers and are likely needed to provide H bonds and serve as proton acceptors during O–O bond formation, (3) re-interpretation of vibration at ~833 cm^{-1} [30] as the terminal peroxide (instead of bridging) is possible (see Table 2), (4) the EXAFS Co–O distance (~1.67 Å) does not agree with the ~1.75 Å Co–O distance predicted for clusters with two Co-oxo fragments, (5) DFT calculations show a large energy penalty for complete acetate dissociation with generation of two Co^{IV}=O units pre-positioned for RC (Equation S1), and (6) formation of this bridging peroxide as a result of earlier discussed Ac/OH exchange[30] seems improbable given that it would require OH groups in *cis* configuration without complete detachment of an acetate (Figure S7), which is a complex structural re-arrangement.

The formation of $[Co^{III}{}_2O_4Co^{IV}$=O/$Co^{IV}(CH_3CO_2)_{mono}]^0$ is straightforward and does not require complete acetate detachment or large conformational re-arrangements

Please cite this article in press as: Ezhov et al., Do multinuclear 3d metal catalysts achieve O–O bond formation via radical coupling or via water nucleophilic attack? WNA leads the way in $[Co_4O_4]^{n+}$, Chem Catalysis (2021), https://doi.org/10.1016/j.checat.2021.03.013

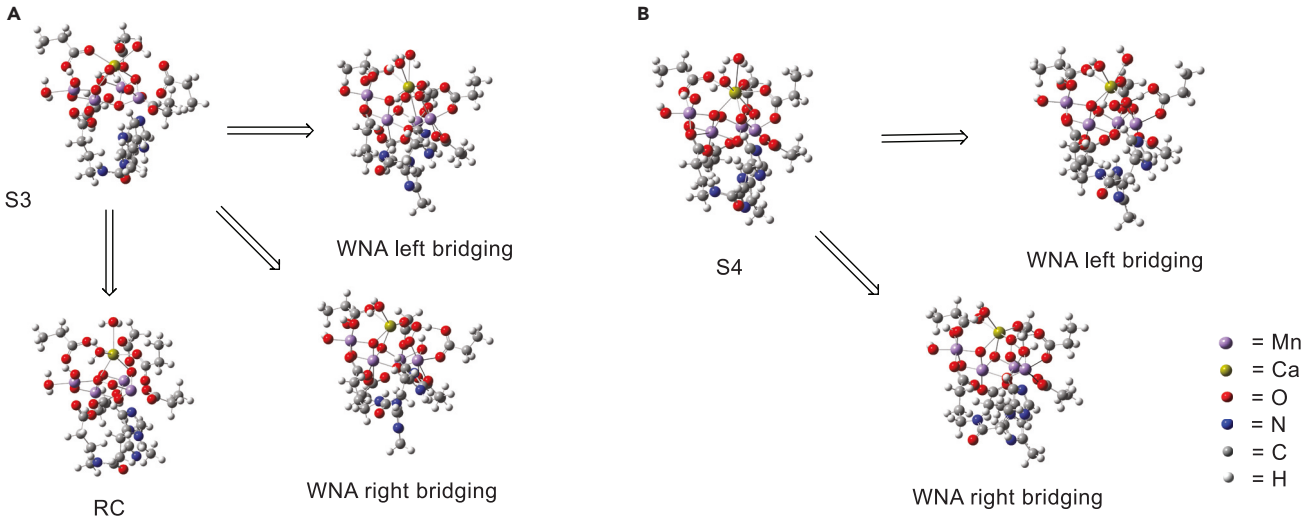

Figure 4. Models of the PS II OEC

Models of the PS II OEC at the S_3 (A) and S_4 (B) states. Structures of the peroxides formed via RC and WNA are shown.

of Co_4O_4 ligands. These species can react with water (or with hydroxide ion) via WNA (Table 1).

Comparative analysis of (1) and PS II OEC O–O bond-formation mechanisms

A strong motivation to study the Co_4O_4 cubane was its resemblance to the $CaMn_4O_5$ cluster of PS II photosynthetic enzyme.[28,62,63] In 2015, we proposed Mn^{IV}=O as a reactive fragment of the S_3 state of the OEC able to satisfy spectroscopic properties and be positioned to form O–O bonds early in the S_3 to S_0 transition (Figure 4A).[57,64,65] Time-resolved X-ray diffraction (TR-XRD) analysis of the S_3 state[66–68] resulted in data that might be interpreted as a formation of at least three possible structures: Mn^{IV}–OH, Mn–OO–Mn, or Mn^{IV}=O, with the last one favored in the most recent study.[66] Interestingly, $[Co^{III}{}_2O_4Co^{IV}{=}O/Co^{IV}(CH_3CO_2)_{mono}]^0$ displays strong radicaloid character for the oxygen in the Co^{IV}=O group (see spin density; Figure 1D). Similar radicaloid character of the Ru^{V}=O fragment oxygen was established via direct spin-density mapping by EPR for the water oxidation intermediate in the "blue dimer" catalyst.[69] In PS II, the O–O bond was proposed to form via RC between the oxygens in Mn^{IV}=O and bridging Mn–O–Mn.[57,70] The mechanism observed for the $[Co^{III}{}_2O_4Co^{IV}{=}O/Co^{IV}(CH_3CO_2)_{mono}]^0$ with involvement of the carboxylate and bridging oxygen as proton acceptors in the O–O bond formation (Figure 1D) prompted analysis of similar configurations for the OEC (Figure 4). The S_3-state model allows WNA of the Ca^{2+}-bound H_2O on the Mn^{IV}=O. The closest carboxylate ligand able to accept a proton is E189, while two oxo bridges, the left (approximately +0.2 eV) and the right (approximately +1.5 eV), of the Mn^{IV}=O fragment may form H bonds with the peroxides formed (Figure 4B). Such peroxides are energetically plausible for formation, even at S_3 state. Note that formation of a peroxide via RC will agree better with the TR-XRD data of the S_3 state because this does not require additional oxygen atoms except those already detected in TR-XRD.[66,68] To account for peroxides formed via WNA on the Mn^{IV}=O, additional oxygen density should be present in the S_3 state (Figure 4A). Thus, such a peroxide can be possible only as a minor configuration. One-electron oxidation of the OEC forming the S_4 state results in similar energetics with approximately +1.8 eV for the left and approximately +0.2 eV for the right (Figure 4B and Table S9).

Future detection of electron densities in the S_4 state (formed ~200–1,000 μs into the S_3-to-S_0 transition) will help to discriminate between RC and WNA mechanisms.

Conclusions

Understanding the exact mechanism of the O–O bond formation requires determination of which of the two main pathways, the RC or the WNA, is operational under reaction conditions. Often, the simple presence of multiple metal centers with the possibility of adjacent M^{n+}=O units is sufficient to sway researchers into proposing the RC pathway with little experimental evidence. Here, we analyzed all available experimental data on the most studied 3d multinuclear WOC, $[Co_4O_4Ac_4Py_4]^0$. We augment earlier results with *in situ* detection of the short, ~1.67 Å, Co^{IV}=O bond crucial to initiate O–O bond formation. The "oxo wall" effect is most likely mitigated here by the multimetallic nature of the $[Co_4O_4]$ cluster. X-ray spectroscopy data and DFT calculations indicate that under electrochemical conditions O–O bond formation proceeds via rate-limiting WNA on $[Co^{III}{}_2O_4Co^{IV}{=}O/Co^{IV}(CH_3CO_2)\text{-}_{mono}]^0$. Formation of Co^V has not been supported experimentally or with DFT. We show that multimetallic cubane provides unique stabilization for the Co^{IV}=O + H_2O = Co–OOH + H^+ transition, with the carboxyl accepting the proton and the bridging oxygen stabilizing the peroxide via H bonding. A similar pathway was identified for the $CaMn_4O_5$ cluster of PS II, which strengthens understanding of the water oxidation mechanisms for both systems. These results inform rational design of multinuclear, 3d transition-metal-based water oxidation catalysts.

EXPERIMENTAL PROCEDURES

Resource availability

Lead contact

Further information and requests for resources should be directed to and will be fulfilled by the lead contact, Yulia Pushkar (ypushkar@purdue.edu).

Materials availability

All unique reagents generated in this study will be made available on request.

Data and code availability

There is no dataset or code associated with this paper.

Materials and methods

Complex (**1**) was prepared and purified as previously described.[28] UV-vis spectra were recorded on a Varian Cary 300 Bio spectrophotometer. Aqueous solutions were prepared with ultrapure (type 1) water (resistivity 18.2 MΩ·cm at 25°C) from a Q-POD unit of the Milli-Q integral water purification system (Millipore, Billerica, MA, USA). XAS measurements were made for BE of (**1**) in water *in situ* in a basic medium at beamline 9 of the Argonne National Laboratory using a potentiostat (CHI 627C; CH Instruments) and a custom-made double-compartment three-electrode cell. The electrolysis of (**1**) was performed in 0.1 M sodium sulfate water solution basified with an appropriate amount of sodium hydroxide to pH 12 for at least 8 h. The cell was equipped with Grafoil as the working electrode, Pt wire as the counter-electrode in an auxiliary chamber filled with the electrolyte solution, and Ag/AgCl as the reference electrode at 1.4 V versus Ag/AgCl applied potential and a 4 μm polypropylene tape window on the X-ray path. The basicity of the solutions in the cell and auxiliary chamber was measured after each scan and adjusted to pH 12 with 1 M NaOH or HNO_3 if necessary. Electrochemical measurements that did not take place at the beamline were performed using a Biologic VSP potentiostat with a typical three-electrode cell: glassy carbon working electrode, Pt wire counterelectrode,

Please cite this article in press as: Ezhov et al., Do multinuclear 3d metal catalysts achieve O–O bond formation via radical coupling or via water nucleophilic attack? WNA leads the way in $[Co_4O_4]^{n+}$, Chem Catalysis (2021), https://doi.org/10.1016/j.checat.2021.03.013

and Ag/AgCl reference electrode. The medium was 0.1 M tetrabutylammonium hexafluorophosphate in acetonitrile, and the measurements were performed under N_2 atmosphere. The data are referenced to the experimentally determined ferrocene redox couple.

X-band EPR measurements were conducted at a temperature of 20 K with a Bruker EMX X-band spectrometer and CW microwave radiation using a ColdEdge closed-cycle cryostat. Power dependence was measured for all detected EPR signals. We found that none of the Co signals could be saturated with maximum available microwave power of 30 mW.

All reported measurements were repeated several times to ensure the reproducibility of the results.

Sample preparation for XAS and EXAFS study of WOR catalyzed by (1) in acidic media

At room temperature, 20 μL of a 200 mM solution of the oxidizer (Ce^{IV}, 20 equiv) in 0.1 M nitric acid was added quickly to an aliquot of 200 μL of 1 mM solution of (**1**) in a mixture of acetonitrile and 0.2 M nitric acid 1:1 by volume. After quick mixing, 40 μL of the reaction mixture was immediately placed into polycarbonate (Lexan) tape-supported polypropylene cryostat sample holders (inner dimensions of 12 × 2 × 3 mm) and frozen in liquid N_2 within 30 s.

Sample preparation for EPR

The EPR samples were prepared by mixing 200 μL of 1 mM (**1**) in 0.1 M HNO_3 with an appropriate amount of Ce^{IV} in an EPR tube or by collecting 200 μL from a working electrochemical cell, followed by freezing in liquid N_2 in less than 30 s.

DFT calculations

The DFT calculations, optimizations, and resulting single-point frequency calculations were performed by Gaussian 16 with unrestricted BP86 Becke's 1988 functional[71] and the gradient corrections of Perdew.[72] The basis set def2tzvp was used for all atoms unless noted otherwise. The CPCM polarizable conductor model was used to model acetonitrile or water solvation. DFT calculations were performed on species relevant to redox reactions, seen in Table S2. DFT was used to optimize geometry and then calculate vibrations and energies. Free energies of reaction, shown in Table S3, were computed on the basis of the energies of these optimized structures. The value of the reference potential (RHE) was assigned to 4.44 V and the free energy of a solvated proton to −11.64 V.[73] For reactions in acetonitrile solution, the value of RHE was assigned to ~5.0 V.

Transition-state calculations were performed with the B3LYP hybrid functional and the def2tzvp basis set for Co and 6-31G* for C, H, N, and O atoms (Table S7 and Video S1). Transition states were identified by the presence of one negative frequency. Transition-state barrier and associated ΔG values were obtained by repeating optimizations and single-point frequency calculations on the reactant and product in this basis set. Obtained energies for transition state were approximately +0.96 eV for BP86/def2tzvp and approximately +0.93 eV for B3LYP/Co-def2tzvp/O, N, C, H (6-31G*) (Tables S6 and S7). This value is similar to previous DFT studies involving WNA on transition metal=O species.[74–82] Note that the reactant and product species in this reaction, $Co^{III}{}_2O_4Co^{IV}$=O/$Co^{IV}(CH_3CO_2)_{mono}/H_2O$ and $Co^{III}{}_2O_4Co^{III}$–OOH/$Co^{III}(CH_3CO_2H)_{mono}$, have triplet and singlet spin states, respectively. Single-point energy calculations along the

reaction pathway revealed that the geometry at which the singlet and triplet states have equal energy is farther along the reaction coordinate than the transition state geometry; as such, the transition state was calculated in the triplet state (Figure S6).

Spin states in calculation inputs were defined across each molecule. DFT calculations then localized spins based on the BP86 methodology. Optimized geometries and frequencies reveal spin states that may be observed locally either by spin-density representations or by calculation of Mulliken spin densities on each atom. In the $Co^{III}{}_2O_4Co^{IV}$=O/$Co^{IV}(CH_3CO_2)_{mono}$ state, three of the Co atoms do not have localized spin, while the Co=O group does have localized spin (Figure 1D).

Bond lengths of Co-oxo species may be different depending on the methods and basis sets employed in the DFT calculations. The basis set and methods used were due to good agreement found in the calculated/experimental redox potentials (Table S3) and agreement with coordination distances based on the best XANES fits. Comparisons between methods UBP86 (generalized gradient approximation) and hybrid functional B3LYP necessitate the use of 15% HF exchange in the UBP86 calculations, as B3LYP includes a percentage of HF exchange. Note that while differences in computational methodologies and basis sets may lead to substantial differences in optimized geometries, B3LYP, BP86, and BP86 + 15% HF all produced similar Co=O distances (all within 0.06 Å).

XAS and EXAFS measurements

X-ray absorption spectra were collected at the Advanced Photon Source at the Argonne National Laboratory on bending magnet beamline 9 at electron energy 7,810 eV and average current of 100 mA. The radiation was monochromatized by a Si (110) crystal monochromator. The intensity of the X-rays was monitored by three ion chambers (I_0, I_1, and I_2) and placed before the sample (I_0) and after the sample (I_1 and I_2). I_1 and I_2 were filled with 100% nitrogen. The X-ray energy was calibrated by setting the first maximum in the derivative of the Co metal K-edge XANES spectrum to 7,709 eV. For *in situ* measurements, a custom-made electrochemical cell with a 4 μm Mylar tape window and a magnetic stirrer were placed between the I_0 and the I_1 ion chambers. Because of the high activity of this catalyst, the pH of the electrochemical solution of (**1**) during the BE shifted toward increasing acidity; pH monitoring and basification occurred prior to each X-ray scan, as necessary.

For the measurements of (**1**) oxidized with Ce^{IV} at pH 1, the plastic (Lexan) EXAFS sample holders with frozen solutions were inserted into a cryostat pre-cooled to 20 K. The samples were kept at 20 K in a He atmosphere at ambient pressure. Data were recorded as fluorescence excitation spectra using a 13-element energy-resolving detector. To reduce the risk of sample damage by X-rays, the defocused mode (beam size 1 × 1 mm) was used, and no damage was observed. The shutter was synchronized with the scan software, preventing exposure to X-rays between scans and during spectrometer movements.

SUPPLEMENTAL INFORMATION

Supplemental information can be found online at https://doi.org/10.1016/j.checat.2021.03.013.

ACKNOWLEDGMENTS

This research was supported by the National Science Foundation (CHE-1900476 to Y.P.) and Valparaiso University (P.S.). The use of the Advanced Photon Source, an

Office of Science User Facility operated by the US Department of Energy (DOE) Office of Science by Argonne National Laboratory, was supported by the US DOE under contract DE-AC02-06CH11357. The PNC/XSD (Sector 20) facilities at the Advanced Photon Source and research at these facilities were supported by the US DOE Basic Energy Science program and the Canadian Light Source. Ms. Y. Pineda-Galvan is acknowledged for assistance at the beamline. Access to EPR was provided by the Amy Instrumentation Facility, Department of Chemistry, under the supervision of Dr. Michael Everly. We thank Prof. G.C. Dismukes from Rutgers University for supplying the sample and helpful discussion and Prof. L. Slipchenko from Purdue University for providing computational resources and helpful discussion.

AUTHOR CONTRIBUTIONS

P.S. provided materials; R.E., A.R., and Y.P. conducted the experiments; G.B., A.R., and Y.P. performed DFT calculations and data analysis; and R.E., P.S., G.B., and Y.P. wrote the paper.

DECLARATION OF INTERESTS

The authors declare no competing interests.

Received: January 8, 2021
Revised: February 24, 2021
Accepted: March 30, 2021
Published: May 3, 2021

REFERENCES

1. Glenk, G., and Reichelstein, S. (2019). Economics of converting renewable power to hydrogen. Nat. Energy *4*, 216–222.

2. Shi, Q.R., Zhu, C.Z., Du, D., and Lin, Y.H. (2019). Robust noble metal-based electrocatalysts for oxygen evolution reaction. Chem. Soc. Rev. *48*, 3181–3192.

3. Reier, T., Nong, H.N., Teschner, D., Schlögl, R., and Strasser, P. (2017). Electrocatalytic oxygen evolution reaction in acidic environments – reaction mechanisms and catalysts. Adv. Energy Mater. *7*, 1601275.

4. Wang, J., Cui, W., Liu, Q., Xing, Z., Asiri, A.M., and Sun, X. (2016). Recent progress in cobalt-based heterogeneous catalysts for electrochemical water splitting. Adv. Mater. *28*, 215–230.

5. Nocera, D.G. (2012). The artificial leaf. Acc. Chem. Res. *45*, 767–776.

6. Smith, P.F., Kaplan, C., Sheats, J.E., Robinson, D.M., McCool, N.S., Mezle, N., and Dismukes, G.C. (2014). What determines catalyst functionality in molecular water oxidation? Dependence on ligands and metal nuclearity in cobalt clusters. Inorg. Chem. *53*, 2113–2121.

7. Li, X., and Siegbahn, P.E. (2013). Water oxidation mechanism for synthetic Co-oxides with small nuclearity. J. Am. Chem. Soc. *135*, 13804–13813.

8. Hong, S., Pfaff, F.F., Kwon, E., Wang, Y., Seo, M.-S., Bill, E., Ray, K., and Nam, W. (2014). Spectroscopic capture and reactivity of a low-spin cobalt(IV)-oxo complex stabilized by binding redox-inactive metal ions. Angew. Chem. Int. Ed. *53*, 10403–10407.

9. Pfaff, F.F., Kundu, S., Risch, M., Pandian, S., Heims, F., Pryjomska-Ray, I., Haack, P., Metzinger, R., Bill, E., Dau, H., et al. (2011). An oxocobalt(IV) complex stabilized by Lewis acid interactions with scandium(III) ions. Angew. Chem. Int. Ed. *50*, 1711–1715.

10. Dalle, K.E., Warnan, J., Leung, J.J., Reuillard, B., Karmel, I.S., and Reisner, E. (2019). Electro- and solar-driven fuel synthesis with first row transition metal complexes. Chem. Rev. *119*, 2752–2875.

11. Lyu, F., Wang, Q., Choi, S.M., and Yin, Y. (2019). Noble-metal-free electrocatalysts for oxygen evolution. Small *15*, 1804201.

12. Risch, M., Khare, V., Zaharieva, I., Gerencser, L., Chernev, P., and Dau, H. (2009). Cobalt–oxo core of a water-oxidizing catalyst film. J. Am. Chem. Soc. *131*, 6936–6937.

13. Olshansky, L., Huerta-Lavorie, R., Nguyen, A.I., Vallapurackal, J., Furst, A., Tilley, T.D., and Borovik, A.S. (2018). Artificial metalloproteins containing Co4O4 cubane active sites. J. Am. Chem. Soc. *140*, 2739–2742.

14. McCool, N.S., Robinson, D.M., Sheats, J.E., and Dismukes, G.C. (2011). A Co4O4 "cubane" water oxidation catalyst inspired by photosynthesis. J. Am. Chem. Soc. *133*, 11446–11449.

15. Umena, Y., Kawakami, K., Shen, J.R., and Kamiya, N. (2011). Crystal structure of oxygen-evolving photosystem II at a resolution of 1.9 Å. Nature *473*, 55–60.

16. Evangelisti, F., Güttinger, R., Moré, R., Luber, S., and Patzke, G.R. (2013). Closer to photosystem II: a Co4O4 cubane catalyst with flexible ligand architecture. J. Am. Chem. Soc. *135*, 18734–18737.

17. Cady, C.W., Gardner, G., Maron, Z.O., Retuerto, M., Go, Y.B., Segan, S., Greenblatt, M., and Dismukes, G.C. (2015). Tuning the electrocatalytic water oxidation properties of AB2O4 spinel nanocrystals: a (Li, Mg, Zn) and B (Mn, Co) site variants of LiMn2O4. ACS Catal. *5*, 3403–3410.

18. Gardner, G.P., Go, Y.B., Robinson, D.M., Smith, P.F., Hadermann, J., Abakumov, A., Greenblatt, M., and Dismukes, G.C. (2012). Structural Requirements in lithium cobalt oxides for the catalytic oxidation of water. Angew. Chem. Int. Ed. *51*, 1616–1619.

19. Gardner, G., Al-Sharab, J., Danilovic, N., Go, Y.B., Ayers, K., Greenblatta, M., and Dismukes, G.C. (2016). Structural basis for differing electrocatalytic water oxidation by the cubic, layered and spinel forms of lithium cobalt oxides. Energy Environ. Sci. *9*, 184–192.

20. Song, F., Moré, R., Schilling, M., Smolentsev, G., Azzaroli, N., Fox, T., Luber, S., and Patzke, G.R. (2017). {Co4O4} and {CoxNi4–xO4} cubane water oxidation catalysts as surface cut-outs of cobalt oxides. J. Am. Chem. Soc. *139*, 14198–14208.

21. Symes, M.D., Surendranath, Y., Lutterman, D.A., and Nocera, D.G. (2011). Bidirectional

and unidirectional PCET in a molecular model of a cobalt-based oxygen-evolving catalyst. J. Am. Chem. Soc. *133*, 5174–5177.

22. Symes, M.D., Lutterman, D.A., Teets, T.S., Anderson, B.L., Breen, J.J., and Nocera, D.G. (2013). Photo-active cobalt cubane model of an oxygen-evolving catalyst. ChemSusChem *6*, 65–69.

23. Brodsky, C.N., Hadt, R.G., Hayes, D., Reinhart, B.J., Li, N., Chen, L.X., and Nocera, D.G. (2017). In situ characterization of cofacial Co(IV) centers in Co4O4 cubane: modeling the high-valent active site in oxygen-evolving catalysts. Proc. Nat. Acad. Sci. USA *114*, 3855–3860.

24. Fernando, A., and Aikens, C.M. (2015). Reaction pathways for water oxidation to molecular oxygen mediated by model cobalt oxide dimer and cubane catalysts. J. Phys. Chem. C *119*, 11072–11085.

25. Du, P., Kokhan, O., Chapman, K.W., Chupas, P.J., and Tiede, D.M. (2012). Elucidating the domain structure of the cobalt oxide water splitting catalyst by X-ray pair distribution function analysis. J. Am. Chem. Soc. *134*, 11096–11099.

26. Ullman, A.M., Liu, Y., Huynh, M., Bediako, D.K., Wang, H., Anderson, B.L., Powers, D.C., Breen, J.J., Abruña, H.D., and Nocera, D.G. (2014). Water oxidation catalysis by Co(II) impurities in Co(III)4O4 cubanes. J. Am. Chem. Soc. *136*, 17681–17688.

27. Nguyen, A.I., Ziegler, M.S., Oña-Burgos, P., Sturzbecher-Hohne, M., Ki, W., Bellone, D.E., and Tilley, T.D. (2015). Mechanistic investigations of water oxidation by a molecular cobalt oxide analogue: evidence for a highly oxidized intermediate and exclusive terminal oxo participation. J. Am. Chem. Soc. *137*, 12865–12872.

28. Smith, P.F., Hunt, L., Laursen, A.B., Sagar, V., Kaushik, S., Calvinho, K.U.D., Marotta, G., Mosconi, E., De Angelis, F., and Dismukes, G.C. (2015). Water oxidation by the [Co4O4(OAc)4(py)4](+) cubium is initiated by OH(-) addition. J. Am. Chem. Soc. *137*, 15460–15468.

29. Genoni, A., La Ganga, G., Volpe, A., Puntoriero, F., Di Valentin, M., Bonchio, M., Natali, M., and Sartorel, A. (2015). Water oxidation catalysis upon evolution of molecular Co(iii) cubanes in aqueous media. Faraday Discuss *185*, 121–141.

30. Liu, H., and Frei, H. (2020). Observation of O–O bond forming step of molecular Co4O4 cubane catalyst for water oxidation by rapid-scan FT-IR spectroscopy. ACS Catal. *10*, 2138–2147.

31. McAlpin, J.G., Stich, T.A., Ohlin, C.A., Surendranath, Y., Nocera, D.G., Casey, W.H., and Britt, R.D. (2011). Electronic structure description of a [Co(III)3Co(IV)O4] cluster: a model for the paramagnetic intermediate in cobalt-catalyzed water oxidation. J. Am. Chem. Soc. *133*, 15444–15452.

32. Nguyen, A.I., Van Allsburg, K.M., Terban, M.W., Bajdich, M., Oktawiec, J., Amtawong, J., Ziegler, M.S., Dombrowski, J.P., Lakshmi, K.V., Drisdell, W.S., et al. (2019). Stabilization of reactive Co4O4 cubane oxygen-evolution catalysts within porous frameworks. Proc. Natl. Acad. Sci. USA *116*, 11630–11639.

33. Ullman, A.M., Brodsky, C.N., Li, N., Zheng, S.L., and Nocera, D.G. (2016). Probing edge site reactivity of oxidic cobalt water oxidation catalysts. J. Am. Chem. Soc. *138*, 4229–4236.

34. Brodsky, C.N., Bediako, D.K., Shi, C., Keane, T.P., Costentin, C., Billinge, S.J.L., and Nocera, D.G. (2019). Proton–electron conductivity in thin films of a cobalt–oxygen evolving catalyst. ACS Appl. Energy Mater. *2*, 3–12.

35. Pasquini, C., Zaharieva, I., González-Flores, D., Chernev, P., Mohammadi, M.R., Guidoni, L., Smith, R.D.L., and Dau, H. (2019). H/D isotope effects reveal factors controlling catalytic activity in Co-based oxides for water oxidation. J. Am. Chem. Soc. *141*, 2938–2948.

36. Hadt, R.G., Hayes, D., Brodsky, C.N., Ullman, A.M., Casa, D.M., Upton, M.H., Nocera, D.G., and Chen, L.X. (2016). X-ray spectroscopic characterization of Co(IV) and metal-metal interactions in Co4O4: electronic structure contributions to the formation of high-valent states relevant to the oxygen evolution reaction. J. Am. Chem. Soc. *138*, 11017–11030.

37. Zhang, M., de Respinis, M., and Frei, H. (2014). Time-resolved observations of water oxidation intermediates on a cobalt oxide nanoparticle catalyst. Nat. Chem. *6*, 362–367.

38. Andris, E., Navrátil, R., Jašík, J., Srnec, M., Rodríguez, M., Costas, M., and Roithová, J. (2019). M-O bonding beyond the oxo wall: spectroscopy and reactivity of cobalt(III)-Oxyl and cobalt(III)-Oxo complexes. Angew. Chem. Int. Ed. *58*, 9619–9624.

39. Wang, B., Lee, Y.-M., Tcho, W.-Y., Tussupbayev, S., Kim, S.-T., Kim, Y., Seo, M.S., Cho, K.-B., Dede, Y., Keegan, B.C., et al. (2017). Synthesis and reactivity of a mononuclear non-haem cobalt(IV)-oxo complex. Nat. Commun. *8*, 14839.

40. Blakemore, J.D., Crabtree, R.H., and Brudvig, G.W. (2015). Molecular catalysts for water oxidation. Chem. Rev. *115*, 12974–13005.

41. McAlpin, J.G., Surendranath, Y., Dincă, M., Stich, T.A., Stoian, S.A., Casey, W.H., Nocera, D.G., and Britt, R.D. (2010). EPR evidence for Co(IV) species produced during water oxidation at neutral pH. J. Am. Chem. Soc. *132*, 6882–6883.

42. Ezhov, R., Ravari, A.K., and Pushkar, Y. (2020). Characterization of the Fe-V=O complex in the pathway of water oxidation. Angew. Chem. Int. Ed. *59*, 13502–13505.

43. Fan, L., Zhang, B., Timmer, B.J.J., Dharanipragada, N.V.R.A., Sheng, X., Tai, C.-W., Zhang, F., Liu, T., Meng, Q., Inge, A.K., and Sun, L. (2020). Promoting the Fe(VI) active species generation by structural and electronic modulation of efficient iron oxide based water oxidation catalyst without Ni or Co. Nano Energy *72*, 104656.

44. Zhang, M., and Frei, H. (2017). Water oxidation mechanisms of metal oxide catalysts by vibrational spectroscopy of transient intermediates. Annu. Rev. Phys. Chem. *68*, 209–231.

45. Hunter, B.M., Gray, H.B., and Muller, A.M. (2016). Earth-abundant heterogeneous water oxidation catalysts. Chem. Rev. *116*, 14120–14136.

46. Mesa, C.A., Francàs, L., Yang, K.R., Garrido-Barros, P., Pastor, E., Ma, Y., Kafizas, A., Rosser, T.E., Mayer, M.T., Reisner, E., et al. (2020). Multihole water oxidation catalysis on haematite photoanodes revealed by operando spectroelectrochemistry and DFT. Nat. Chem. *12*, 82–89.

47. Wang, L.-P., and Van Voorhis, T. (2011). Direct-coupling O2 bond forming a pathway in cobalt oxide water oxidation catalysts. J. Phys. Chem. Lett. *2*, 2200–2204.

48. Hodel, F.H., and Luber, S. (2016). What influences the water oxidation activity of a bioinspired molecular CoII4O4 cubane? An in-depth exploration of catalytic pathways. ACS Catal. *6*, 1505–1517.

49. King, H.J., Fournier, M., Bonke, S.A., Seeman, E., Chatti, M., Jumabekov, A.N., Johannessen, B., Kappen, P., Simonov, A.N., and Hocking, R.K. (2019). Photon-induced, timescale, and electrode effects critical for the in situ X-ray spectroscopic analysis of electrocatalysts: the water oxidation case. J. Phys. Chem. C *123*, 28533–28549.

50. Wang, C.-C., Chang, H.-C., Lai, Y.-C., Fang, H., Li, C.-C., Hsu, H.-K., Li, Z.-Y., Lin, T.-S., Kuo, T.-S., Neese, F., et al. (2016). A structurally characterized nonheme cobalt–hydroperoxo complex derived from its superoxo intermediate via hydrogen atom abstraction. J. Am. Chem. Soc. *138*, 14186–14189.

51. Fukuzumi, S., Lee, Y.-M., and Nam, W. (2019). Structure and reactivity of the first-row d-block metal-superoxo complexes. Dalton Trans. *48*, 9469–9489.

52. Farinas, E., Baidya, N., and Mascharak, P.K. (1994). Electron paramagnetic resonance studies on the formation and decomposition of the oxygenated product of [CoII(PMA)]+, a synthetic analog of cobalt(II) Bleomycin. Inorg. Chem. *33*, 5970–5973.

53. Nguyen, A.I., Wang, J., Levine, D.S., Ziegler, M.S., and Tilley, T.D. (2017). Synthetic control and empirical prediction of redox potentials for Co4O4 cubanes over a 1.4 V range: implications for catalyst design and evaluation of high-valent intermediates in water oxidation. Chem. Sci. *8*, 4274–4284.

54. Wu, J.-Z., Sellitto, E., Yap, G.P.A., Sheats, J., and Dismukes, G.C. (2004). Trapping an elusive intermediate in Manganese−Oxo cubane Chemistry. Inorg. Chem. *43*, 5795–5797.

55. Dogutan, D.K., McGuire, R., Jr., and Nocera, D.G. (2011). Electocatalytic water oxidation by cobalt(III) Hangman b-Octafluoro corroles. J. Am. Chem. Soc. *133*, 9178–9180.

56. Dimitrou, K., Brown, A.D., Concolino, T.E., Rheingold, A.L., and Christou, G. (2001). Mixed-valence, tetranuclear cobalt(,) complexes: preparation and properties of [CoO(OCR)(bpy)] salts. Chem. Comm. 1284–1285.

57. Pushkar, Y., Davis, K.M., and Palenik, M. (2018). Model of the oxygen evolving complex which is highly predisposed to O–O bond formation. J. Phys. Chem. Lett. *9*, 3524–3531.

58. Siegbahn, P.E.M. (2008). A structure-consistent mechanism for dioxygen formation in photosystem II. Chem. Eur. J. *14*, 8290–8302.

59. Yamaguchi, K., Shoji, M., Isobe, H., Yamanaka, S., Kawakami, T., Yamada, S., Katouda, M., and Nakajima, T. (2018). Theory of chemical bonds in metalloenzymes XXI. Possible mechanisms of water oxidation in oxygen evolving complex of photosystem II. Mol. Phys. *116*, 717–745.

60. Yulia Pushkar, Y.P.-G., Ravari, A.K., Otroshchenko, T., and Hartzler, D.A. (2018). Mechanism for O–O bond formation via radical coupling of metal and ligand based radicals: a new pathway. J. Am. Chem. Soc. *140*, 13538–13541.

61. Zhan, S., De Gracia Triviño, J.A., and Ahlquist, M.S.G. (2019). The carboxylate ligand as an oxide relay in catalytic water oxidation. J. Am. Chem. Soc. *141*, 10247–10252.

62. Pantazis, D.A. (2019). The S-3 state of the oxygen-evolving complex: overview of spectroscopy and XFEL crystallography with a critical evaluation of early-onset models for O-O bond formation. Inorganics *7*, 30.

63. Lee, C., and Aikens, C.M. (2015). Water splitting processes on Mn4O4 and CaMn3O4 model cubane systems. J. Phys. Chem. A. *119*, 9325–9337.

64. Davis, K.M., Sullivan, B.T., Palenik, M.C., Yan, L., Purohit, V., Robison, G., Kosheleva, I., Henning, R.W., Seidler, G.T., and Pushkar, Y. (2018). Rapid evolution of the photosystem II electronic structure during water splitting. Phys. Rev. X *8*, 041014.

65. Davis, K.M., Sullivan, B.T., Palenik, M.C., Yan, L., Purohit, V., Robison, G., Kosheleva, I., Henning, R.W., Seidler, G.T., and Pushkar, Y. (2015). Rapid evolution of the photosystem II electronic structure during water splitting. arXiv, 1506.08862. https://doi.org/10.1103/PhysRevX.8.041014.

66. Suga, M., Akita, F., Yamashita, K., Nakajima, Y., Ueno, G., Li, H., Yamane, T., Hirata, K., Umena, Y., Yonekura, S., et al. (2019). An oxyl/oxo mechanism for oxygen-oxygen coupling in PSII revealed by an x-ray free-electron laser. Science *366*, 334–338.

67. Suga, M., Akita, F., Sugahara, M., Kubo, M., Nakajima, Y., Nakane, T., Yamashita, K., Umena, Y., Nakabayashi, M., Yamane, T., et al. (2017). Light-induced structural changes and the site of O=O bond formation in PSII caught by XFEL. Nature *543*, 131–135.

68. Kern, J., Chatterjee, R., Young, I.D., Fuller, F.D., Lassalle, L., Ibrahim, M., Gul, S., Fransson, T., Brewster, A.S., Alonso-Mori, R., et al. (2018). Structures of the intermediates of Kok's photosynthetic water oxidation clock. Nature *563*, 421–425.

69. Moonshiram, D., Alperovich, I., Concepcion, J.J., Meyer, T.J., and Pushkar, Y. (2013). Experimental demonstration of radicaloid character in a Ru-V=O intermediate in catalytic water oxidation. Proc. Natl. Acad. Sci. USA *110*, 3765–3770.

70. Siegbahn, P.E.M. (2013). Water oxidation mechanism in photosystem II, including oxidations, proton release pathways, O-O bond formation and O-2 release. Biochim. Biophys. Acta-bioenerg. *1827*, 1003–1019.

71. Becke, A.D. (1988). Density-functional exchange-energy approximation with correct asymptotic behavior. Phys. Rev. A. *38*, 3098–3100.

72. Perdew, J.P., and Yue, W. (1986). Accurate and simple density functional for the electronic exchange energy: generalized gradient approximation. Phys. Rev. B *33*, 8800–8802.

73. Pushkar, Y., Moonshiram, D., Purohit, V., Yan, L., and Alperovich, I. (2014). Spectroscopic analysis of catalytic water oxidation by [RuII(bpy)(tpy)H2O]2+ suggests that RuV=O is not a rate-limiting intermediate. J. Am. Chem. Soc. *136*, 11938–11945.

74. Tong, L., Inge, A.K., Duan, L., Wang, L., Zou, X., and Sun, L. (2013). Catalytic water oxidation by mononuclear Ru complexes with an anionic ancillary ligand. Inorg. Chem. *52*, 2505–2518.

75. Sala, X., Ertem, M.Z., Vigara, L., Todorova, T.K., Chen, W., Rocha, R.C., Aquilante, F., Cramer, C.J., Gagliardi, L., and Llobet, A. (2010). The cis-[RuII(bpy)2(H2O)2]2+ water-oxidation catalyst revisited. Angew. Chem. Int. Ed. *49*, 7745–7747.

76. Angeles-Boza, A.M., Ertem, M.Z., Sarma, R., Ibañez, C.H., Maji, S., Llobet, A., Cramer, C.J., and Roth, J.P. (2014). Competitive oxygen-18 kinetic isotope effects expose O–O bond formation in water oxidation catalysis by monomeric and dimeric ruthenium complexes. Chem. Sci. *5*, 1141–1152.

77. Vigara, L., Ertem, M.Z., Planas, N., Bozoglian, F., Leidel, N., Dau, H., Haumann, M., Gagliardi, L., Cramer, C.J., and Llobet, A. (2012). Experimental and quantum chemical characterization of the water oxidation cycle catalysed by [RuII(damp)(bpy)(H2O)]2+. Chem. Sci. *3*, 2576–2586.

78. Li, Y.-Y., Tong, L.-P., and Liao, R.-Z. (2018). Mechanism of water oxidation catalyzed by a mononuclear iron complex with a square polypyridine ligand: a DFT study. Inorg. Chem. *57*, 4590–4601.

79. Privalov, T., Åkermark, B., and Sun, L. (2011). The O-O bonding in water oxidation: the electronic structure portrayal of a concerted oxygen atom-proton transfer pathway. Chemistry *17*, 8313–8317.

80. Shao, Y., de Groot, H.J.M., and Buda, F. (2019). Proton acceptor near the active site lowers dramatically the O–O bond formation energy barrier in photocatalytic water splitting. J. Phys. Chem. Lett. *10*, 7690–7697.

81. Hughes, T.F., and Friesner, R.A. (2011). Systematic investigation of the catalytic cycle of a single site ruthenium oxygen evolving complex using density functional theory. J. Phys. Chem. B *115*, 9280–9289.

82. Rudshteyn, B., Fisher, K.J., Lant, H.M.C., Yang, K.R., Mercado, B.Q., Brudvig, G.W., Crabtree, R.H., and Batista, V.S. (2018). Water-nucleophilic attack mechanism for the CuII(pyalk)2 water-oxidation catalyst. ACS Catal. *8*, 7952–7960.